A Sub-400-nT/$\sqrt{\text{Hz}}$, 775-μW, Multi-Loop MEMS Magnetometer With Integrated Readout Electronics

Paolo Minotti, Stefano Brenna, *Member, IEEE*, Giacomo Laghi, Andrea G. Bonfanti, *Member, IEEE*, Giacomo Langfelder, *Member, IEEE*, and Andrea L. Lacaita, *Fellow, IEEE*

I. Introduction

MICROELECTROMECHANICAL system (MEMS) based Lorentz force magnetometers are attracting increasing interest for several reasons [1]. Compared to existing anisotropic magneto-resistance (AMR) or Hall-effect devices, they enable the fabrication of single-process, single-chip 9-axis Inertial Measurement Units (IMUs); they show almost unlimited full-scale (compared to typical needs for consumer applications), without any intrinsic sensitivity vs full-scale trade-off typical e.g. of AMR devices [2]; they enable the realization of fully planar 3-axis devices (planar 3-axis AMR devices require the use of magnetic concentrators [3]); they avoid the use of magnetic materials; they overcome noise densities reachable by Hall devices [4]. The performances of a magnetic field sensing system based on a Lorentz-force MEMS, in terms of resolution, linear full-scale range and bandwidth, depend on the micromachined device, on its packaging, and on the readout electronics. Currently, only a few works have addressed integrated electronics for Lorentz-force MEMS magnetometers [1].

Concerning the MEMS sensing element and its operation, most works exploited AC currents injected at the device resonance frequency (*resonant operation*) to amplify the Lorentz-force induced motion with a high quality factor [5]–[9]. In other words, the magnetic field induces, through the Lorentz force, an amplitude modulation (AM) of the resonant displacement of the MEMS suspended frame (this operating scheme resembles open-loop operation in mode-matched gyroscopes [10]). Critical drawbacks of this kind of operation are a trade-off between the achievable bandwidth and resolution [11], the challenges of tracking the device resonance without large offsets, and the sensitivity long-term stability, affected by the Q-factor dependence on temperature. Current chopping was proposed as a technique to reduce offset and associated drifts [9]. Force-rebalanced MEMS magnetometers were recently investigated in the literature [12]. With this implementation, the temperature dependence of the scale factor is reduced and wide bandwidths can be achieved.

Few approaches alternative to the Lorentz force principle were proposed for MEMS magnetometers: in [13] electromagnetic induction is described, which however requires up to 50 V and works in the hundred-mT range rather than around the Earth field range. In [14] the authors exploit a CoFe/PtMn stack on top of suspended parts, a concept that loses the advantages of avoiding magnetic materials. The focus is thus set on Lorentz-force devices operated in alternative modes with respect to AM resonant operation.

Frequency modulated (FM) Lorentz-force magnetometers, first proposed in [15], were recently given attention. This solution has the advantages of no trade-off between bandwidth and quality factor, and improved sensitivity stability with temperature [16]. However, even improving the sensitivity with micro-leverage solutions [17], white noise performance is limited to 20 $\mu\text{T}/\sqrt{\text{Hz}}$ using 6 V of bias of the suspended mass, and 4 mA of driving current. Assuming a circuit supply of 3 V, this turns into more than 12 mW of overall power dissipation (which can be markedly different with respect to Joule dissipation in the device only). This is largely out of consumer-application specifications. Furthermore, long-term offset stability is affected by frequency changes with temperature.

Another way to overcome both trade-offs between resolution and bandwidth, and long-term stability issues

Manuscript received May 20, 2015; revised June 15, 2015; accepted June 19, 2015. Date of publication July 20, 2015; date of current version November 25, 2015. This work was supported by the European Community through the European Nanoelectronics Initiative Advisory Council Nanoelectronics Framework Programme under Grant Lab4MEMS 325622-2. Subject Editor A. Seshia.

The authors are with the Dipartimento di Elettronica, Informazione e Bioingegneria, Politecnico di Milano, Milan 20133, Italy (e-mail: paolo.minotti@polimi.it; stefano.brenna@polimi.it; giacomo.laghi@polimi.it; andrea.bonfanti@polimi.it; giacomo.langfelder@polimi.it; andrea.lacaita@polimi.it).

Color versions of one or more of the figures in this paper are available online.

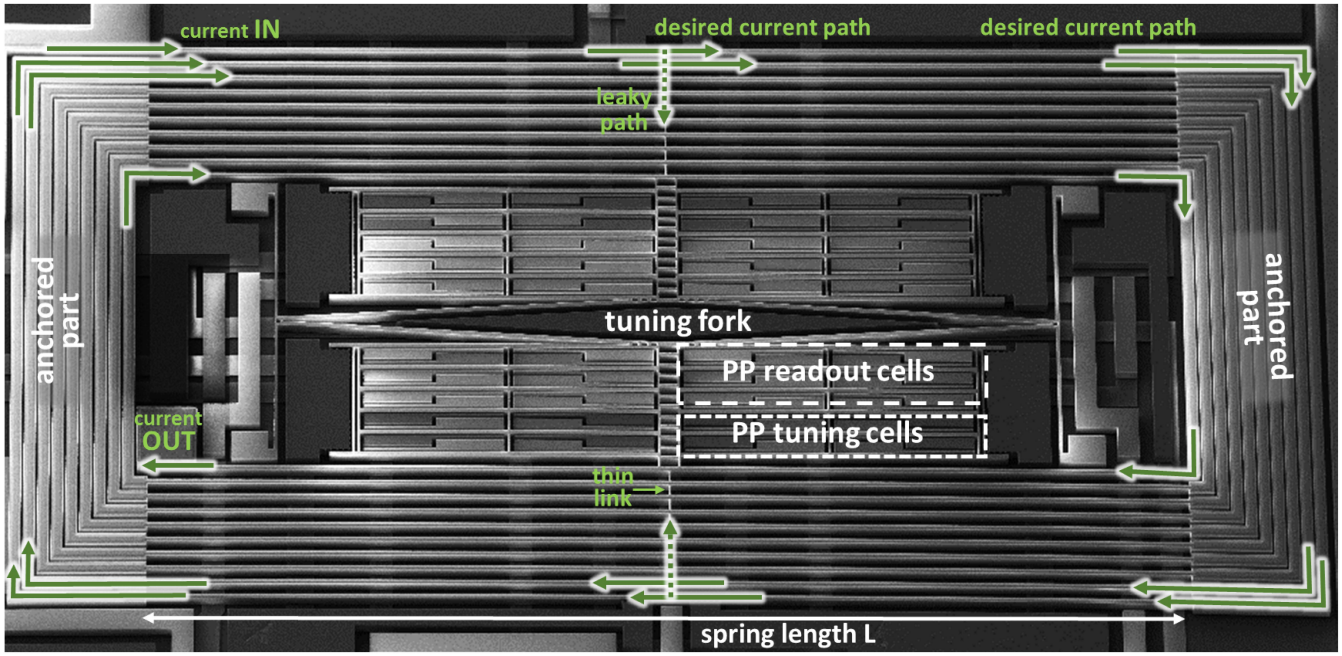

Fig. 1. SEM photograph of the device showing the diamond-shaped tuning fork, the current recirculation concept, implemented through 10 metal coils deposited over the springs, and the parallel plate (PP) cells, used for the capacitive readout and tuning. Solid arrows indicate the desired current flow; dashed arrows indicate examples of possible unwanted leaky paths.

associated to resonant operations, is to drive the magnetometer slightly off-resonance, as often adopted in MEMS gyroscopes [18]–[20]. In this operating mode, the scale-factor becomes independent of the quality factor. Moreover, the scale-factor dependence on resonance frequency variation, induced by temperature changes, is minimized if the reference drive frequency is provided by a MEMS resonator.

A drawback in off-resonance mode is given by its inherent sensitivity loss: the residual gain with respect to DC operation can be in the order of 50, instead of typical Q values between some hundreds and a few thousands.

This work presents a z-axis magnetometer operated off-resonance, with a metal multi-loop structure that helps amplify the Lorentz current effect to recover a high sensitivity in off-resonance operation. The device exploits a direct metal-on-polysilicon deposition step, and it is fabricated with a standard industrial technology process (no added steps).

The sensor is coupled to a 0.35-μm-technology integrated circuit for the readout, which includes a capacitive-sensing front-end, a mixer and a low-pass filter for signal demodulation. The circuit provides the biasing for the capacitive stators (2 V) and requires a current of 150 μA from a 3 V supply. The overall power dissipation, including both the Lorentz current (107 μA_{rms}) and the circuit biasing, is 775 μW only.

In these conditions, a sub 400 nT/$\sqrt{\text{Hz}}$ resolution is obtained, with package pressures in the order of 0.7 mbar, and for a frequency mismatch up to 200 Hz, where the noise contributions of the device and the electronics are designed to match. This allows to obtain a bandwidth of more than 50 Hz, compatible with consumer-application requirements. Large full-scale ranges can be obtained by tuning the driving current. The linearity error, limited by the electronics, is lower than 1% for magnetic fields up to $\pm$2.4 mT, exceeding the full-scale of current devices based on Hall effect or anisotropic magneto-resistance (AMR) [11].

II. Magnetometer Design

This section describes the Lorentz-force-based MEMS magnetometer designed for z-axis magnetic field sensing. With respect to previous implementations in the same process [8], the device exploits a tuning fork geometry, to reject accelerations and vibrations, following what implemented in gyroscopes [21], and the current recirculation loop concept [7], to amplify the sensitivity. The sensor is fabricated using the Thick Epitaxial Layer for Microactuators and Accelerometers (ThELMA) process from STMicroelectronics [8]. All the shown finite element simulation (FEM) results were obtained using full 3-D geometries in *Comsol Multiphysics*, with at least five elements within the smallest dimension of every structural part.

A. Mechanical Simulations and Design

The sensor mechanical part is made of two springs, each formed by ten beams of length L, holding a suspended frame (rotor). The beams of each spring are connected through thin links. The frame faces two nested pairs of fixed electrodes, defining a set of differential parallel plate capacitors. Fig. 1 is a scanning electron microscope (SEM) photograph of the device. As described in more details in the following, the current i flows through the two (top and bottom) springs in opposite directions, so that a z-component of the magnetic field gives rise to in-plane, opposite Lorentz forces F: the frame is therefore split into two symmetric sub-frames, coupled

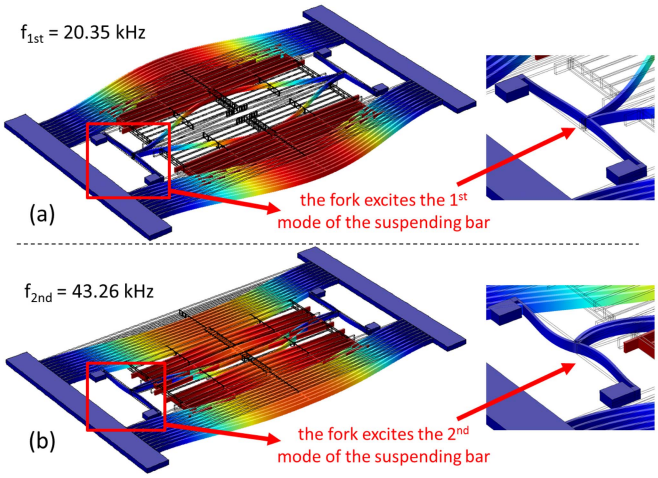

Fig. 2. Results of FEM simulations for (a) the anti-phase mode, excited by the Lorentz current flowing in opposite directions through the springs, and for (b) the in-phase mode, excited by external accelerations. The insets show how the tuning-fork geometry, coupled to the holding bars, helps in shifting the in-phase mode to frequencies higher than for the anti-phase mode.

through a tuning-fork spring. The presence of the tuning-fork determines the existence of both an in-phase and an anti-phase in-plane translational modes. The opposite direction of the Lorentz current excites the anti-phase mode, whose shape is indicated in the eigen-frequency FEM simulation of Fig. 2a. The detection of the magnetic field B is obtained through suitably arranged differential parallel plates formed by the fixed electrodes facing the frame.

On the contrary, an external acceleration causes concordant forces for the two sub-frames (see the in-phase mode FEM simulation, Fig. 2b). In this way, the action generated by the magnetic field results in a differential signal, while external accelerations are ideally rejected and, to first order, do not provide any differential capacitance variations. This approach is to be pursued because the Lorentz force (like the Coriolis force in gyroscopes) can be orders of magnitude smaller than inertial forces.

In order to further decrease effects of accelerations and vibrations, the in-phase mode has a resonance frequency higher than the anti-phase mode. This is obtained thanks to the specific geometry of the tuning fork, formed by a diamond spring and two holding bars [22]. As shown in the two insets of Fig. 2, while the anti-phase motion excites the first mode of the holding bars, the in-phase motion of the sub-frames excites the second mode of the holding bars, and is therefore shifted upwards. The springs and the tuning fork geometry are designed to set the anti-phase drive mode f_0 around 20 kHz, while the in-phase mode falls at about 43 kHz.

B. Electrical Simulations and Design

As described in the Introduction, off-resonance operation implies a decrease of the structure motion compared to resonant operation. A way to recover this signal decrease can be obtained if the current is re-used multiple times through recirculation loops. E.g. for $N = 10$ current loops, a sensitivity increase by a factor 10 is directly obtained.

The definition of the recirculation path required a preliminary evaluation of the technological options available for the deposition of metal layers on the structural polysilicon used for the micro-fabrication. Two options were investigated: (i) the deposition of metal paths isolated from the structural layer through a barrier material (SiC) and (ii) the deposition of metal paths directly on the polysilicon layer. The former option has the obvious advantage of allowing an optimum definition of the current paths, completely decoupling the electrical domain from the mechanical domain. However, it proved to be technologically challenging due to residual stresses on the different materials forming the stack. The second option was therefore selected. The challenge in the design of multiple loops within a standard industrial process, like the one adopted in this work, is thus represented by the absence of an insulating layer between the metal (deposited to form the loops) and the heavily doped polysilicon structural layer.

This challenge can be understood by looking again at Fig. 1: the current enters into the loops on the top-left corner, as shown (IN). The ideal path, represented by the metal deposition, is indicated by the solid arrows (shown only for the first two loops) and is based on recirculation, with an exit on the central-left corner after 10 loops (OUT). However, as there is no isolation between the metal and the structural polysilicon layer, leaky paths can bypass the desired current flow (e.g. as represented by dashed arrows). The device design therefore requires also electrical simulations to predict and optimize the current effectiveness. These simulations account for the nominal resistivity of the 700-nm-thick Al metal layer (0.04 $\Omega_{/\square}$), of the 22-μm-thick polysilicon layer (20.5 $\Omega_{/\square}$), and for the nominal metal-over-poly contact resistance per unit area.

Using the same geometry and software adopted for the mechanical-domain simulations, electrical-domain simulations were performed by applying a fixed voltage difference between the multiple-loop ends. To minimize current leakages, the metal path was designed to have the lowest possible square resistance, increasing the path width, yet compatibly with the beams width and the dimensioning of the anti-phase mode resonance frequency to be set around 20 kHz. In the optimum situation, the nominal beams width is 6 μm, with a nominal metal width on top of them of 5.7 μm and an expected rectangular cross-section. A 0.15 μm per side enclosure value of Al within polysilicon was adopted after discussing with process engineers. For the given data, Fig. 3 reports the current density through the metal loops as a function of the space coordinate along the current path. The reader can note, for the nominal 5.7 μm width, a 19% current decrease within the first loop, occurring through the leaky path represented by the thin, straight, polysilicon links between the spring beams. No significant further decreases along all the other loops are observed, as they partly re-gain the current lost by the first loop. This 19% loss thus reduces the number of effective loops to an average value $N_l \approx 8.1 < N$ (dashed line).

Fig. 4a shows a SEM photograph of the effectively obtained metal-over-poly structure, after the device fabrication. An etching of the metal paths larger than expected leads to a metal width in the order of 3.1 μm. According to the

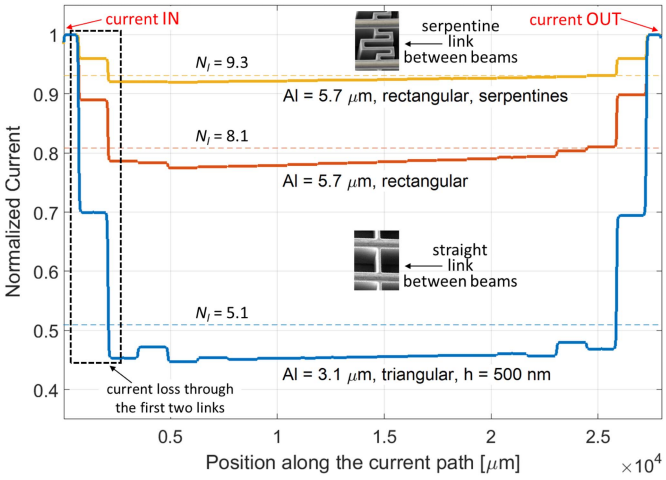

Fig. 3. Simulation for the Lorentz current flowing through the metal loops from the input (x-axis left end) to the output (x-axis right end). The curves refer to different metal widths and cross-sections or to different link geometries. The partial current loss in the first loop decreases if the resistance of the Al path is decreased (wide metal), or when the links resistance increases (serpentines).

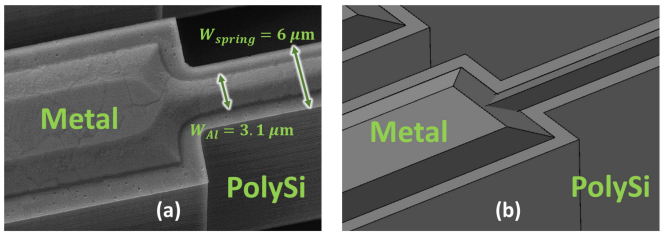

Fig. 4. Details of a SEM photograph showing the metal-over-poly structure at one spring end (a), and the corresponding geometry for the post-fabrication simulations (b).

simulations above, repeated for the actual metal geometry (triangular cross-section with a 500-nm height, see Fig. 4b) the undesired current paths reduce the effective number of loops to a value $N_l \approx 5.1$. This is the value that will be used for sensitivity and resolution predictions in the following of this work. For future implementations, the metal mask will be widened to bypass the excessive Al etching and to minimize the loop resistance. Further, alternative geometries of the thin polySi links, like serpentine structures, are under investigation to increase the resistance of the leaky path, so to maximize to $N_l \approx 9.3$ the loop efficiency (see again Fig. 3 for the predictions on this new geometry with the serpentine structure shown in the inset).

C. Device Packaging and Overall Dimensions

The device has an overall area (excluding the interconnections to the pads) of 1700 μm $\times$ 750 μm. Other parameters are summarized in Table I. The magnetometer is provided with tuning electrodes, used for offset minimization as described in [23].

The sensor is packaged at relatively low pressure (0.75 mbar, the same used for other inertial sensors in this process) to minimize the damping coefficient. In off-resonance operation, this in turn enables thermomechanical

TABLE I
DEVICE PARAMETERS

Parameter	*Value*
Spring length (L)	1400 μm
Nominal thickness (h)	22 μm
Nominal air gap (x_0)	2.1 μm
Nominal rest capacitance (C_0)	420 fF
Nominal package pressure (p)	0.75 mbar
Beam stiffness (from FEM) (k)	80 N/m
Calculated effective mass (m)	5 nkg
Calculated damping coefficient (b)	$8{\cdot}10^{-7}$ N/(m/s)
Anti-phase resonance frequency (from FEM) (f_0)	20.35 kHz
Calculated anti-phase quality factor (Q)	460
In-phase resonance frequency (from FEM) (f_i)	43.26 kHz

noise floor reduction down to the minimum level allowed by the technology without reducing the bandwidth [11], as later described in Section II.E. Considering the nominal 2.1 μm gap between parallel plates, the Knudsen number can be calculated to be well above 10; the corresponding gas regime is thus the free-molecule flow one [24]. In this regime, the dissipation can be assessed by taking into account the interaction between the gas molecules and the device sidewalls, without accounting for the molecule-to-molecule interaction, using boundary models like those discussed in [25]. The so calculated quality factor for the anti-phase mode turns out to be in the order of 460.

D. Prediction and Validation of the Sensitivity

The mechanical sensitivity, i.e. the differential capacitance variation per unit magnetic field change, $S_m = dC_d/dB$, can be estimated as:

$$S_m = \frac{dx}{dB}\frac{dC_d}{dx} = \frac{dF}{dB}\frac{dx}{dF}\frac{dC_d}{dx} = N_l L_{eff} i_0 \cdot \frac{Q_{eff}}{k} \cdot \frac{2C_0}{x_0}, \quad (1)$$

where L_{eff} is the effective length of the springs, that takes into account that the Lorentz force is distributed along the springs and cannot be represented by a point-like force applied to the mass (with our geometry, $L_{eff} \simeq L/2$), i_0 is the AC amplitude of the driving current, Q_{eff} is the effective Q-factor, that represents the displacement amplification with respect to DC operation, k is the spring constant of the device, $C_0 = N_r \varepsilon_0 A/x_0$ is the DC capacitance between the rotor and each stator, N_r being the number of differential parallel plate readout cells, ε_0 being the permittivity inside the package (assumed as that of vacuum), and A their facing area. Finally x_0 is the gap between the rotor and the stators.

For off-resonance mismatches larger than the MEMS intrinsic bandwidth $\Delta f = f_0 - f_d \gg f_0/(2Q)$, the effective Q-factor can be expressed as $Q_{eff} = f_0/(2\Delta f)$ [11]. The mechanical sensitivity can be thus evaluated as:

$$S_m = N_l L_{eff} i_0 \frac{f_0}{k\Delta f}\frac{N_r \varepsilon_0 A}{x_0^2}. \quad (2)$$

The theoretically-calculated value, normalized to the AC current amplitude, is $S_{m,i} = S_m/i_0 = 0.87$ zF/(nT·mA) for an off-resonance split $\Delta f = 200$ Hz. Eq. 2 is derived by assuming that the sensor is driven by a harmonic current with

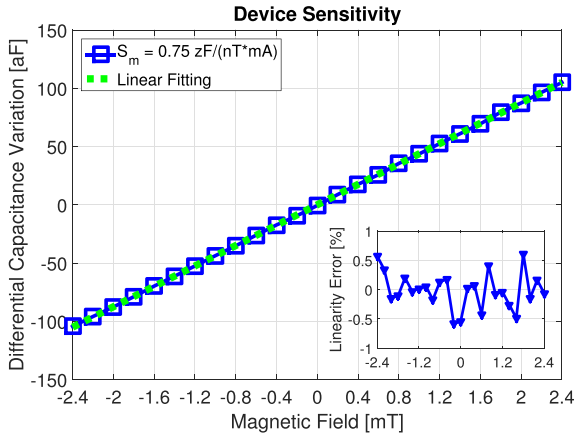

Fig. 5. Mechanical sensitivity of the magnetometer. The blue squares correspond to measurements, the green dotted line is the best linear fitting. The inset shows the linearity error over the full scale range (±2.4 mT).

amplitude i_0 at a frequency $f_d = f_0 - \Delta f$. The differential capacitance variation will be also an AC signal, at the same frequency, with an amplitude equal to $B \cdot S_m$.

For a validation of the predicted sensitivity, before coupling the device to the integrated circuit discussed in the following, a characterization of the inherent device performance was done using a low-noise setup based on discrete electronics and an external lock-in amplifier (SRS830 from Stanford Research Systems). The discrete electronics relies on a pair of charge amplifiers followed by an instrumentation amplifier: the reader can refer to [20] for details about this discrete circuit implementation.

The sensitivity was measured inside a Helmholtz coil magnetic field generator from Micromagnetic Inc., after compensating for the Earth field. Fig. 5 shows the experimental results (blue line, with markers) when sweeping the field between -2.4 mT and 2.4 mT, together with their best linear fitting (green dotted line). The measurements were carried out with an AC current amplitude of 58 μA. The measured normalized sensitivity is 0.75 zF/(nT·mA), showing a 15% deviation from predictions. The difference may be ascribed to deviations between nominal and obtained parameters, e.g. the gap etching between parallel plates, or the metal-over-poly contact resistance. The inset of Fig. 5 also shows the linearity error, defined as the deviation of the measurements from the best fitting line normalized to the full scale range (FSR). As shown, over the whole FSR of ±2.4 mT, the linearity error is lower than 0.6% (actually limited by noise rather than real sensor non-linearity).

E. Prediction of Thermo-Mechanical Noise

Assuming, initially, that resolution is limited by the thermomechanical noise of the device, the minimum detectable magnetic field per unit bandwidth is given by [11]:

$$\sigma_B = \frac{2}{N_l L_{eff} i_0} \sqrt{k_b T b}, \tag{3}$$

where k_b is the Boltzmann constant, T is the absolute temperature and b is the damping coefficient. As mentioned in Section II.C, b was estimated with the model proposed in [24] and [25]. At pressures in the order of 0.75 mbar, the system operates in free-molecule flow regime. Assuming that squeeze-film damping between parallel plates dominates, a damping coefficient per unit facing area $b_a = b/A = 4.9$ (N/(m/s))/m^2 was used. The resolution, normalized per AC current amplitude, i.e. $\sigma_{B,i} = \sigma_B \cdot i_0$, can be estimated as $\sigma_{B,i} = 33$ nT·mA/$\sqrt{\text{Hz}}$.

The output noise, expressed as rms differential capacitance variation per unit bandwidth, can be estimated as:

$$\sigma_C = \sigma_B \cdot S_m = \sqrt{4 k_b T b} \frac{Q_{eff}}{k} \frac{dC_d}{dx}. \tag{4}$$

With the described device and process parameters, this can be evaluated as $\sigma_C = 30$ zF/$\sqrt{\text{Hz}}$, independently of the driving current. This value was taken into account as the target input-referred capacitance noise for the ASIC design described in the following section.

III. Integrated Electronics

AM off-resonance operation is characterized by identical signal-to-noise ratio (SNR) but lower sensor gain than AM resonant sensing [20]. From an electronics design perspective, this implies both a lower input signal and a lower thermomechanical noise (e.g. in terms of rms capacitance variation), as defined by Eq. 2 and Eq. 4. In order not to worsen the SNR, the analog integrated front-end must therefore reach noise levels lower than or comparable to the device noise, even in the described demanding situation. This represents a big challenge in terms of power-noise trade-off.

The capacitive readout circuit described in the following is based on the version proposed in [1] and [26]. With respect to the referenced works, the circuit features custom-designed pads to minimize their parasitic capacitance to ground and associated noise worsening. Further, gain and filtering stages were tailored to the nominal performance of the device of this work. Finally, the integrated circuit shown here also features a Pierce oscillator to be coupled to a MEMS resonator, for the implementation of the reference driving frequency. All the circuits are operated under a 3-V supply voltage.

A simplified schematic of the system is shown in Fig. 6: the readout chain is composed by a cascade of two band-pass amplifiers, a down-conversion mixer, an instrumentation amplifier that transforms the signal from fully-differential to single ended and a g_m-C filter setting the final bandwidth of the system.

A. Amplification Stages

The first stage is a low-noise amplifier (LNA) implemented as a fully-differential charge amplifier with input nodes directly connected to the magnetometer stators. The rotor is assumed to be at ground potential, while the stators are biased at the common-mode input voltage V_{bias} of the LNA that, in turn, is equal to its output common-mode voltage. This voltage value can be externally tuned in order to properly bias the magnetometer and to maximize the signal gain of

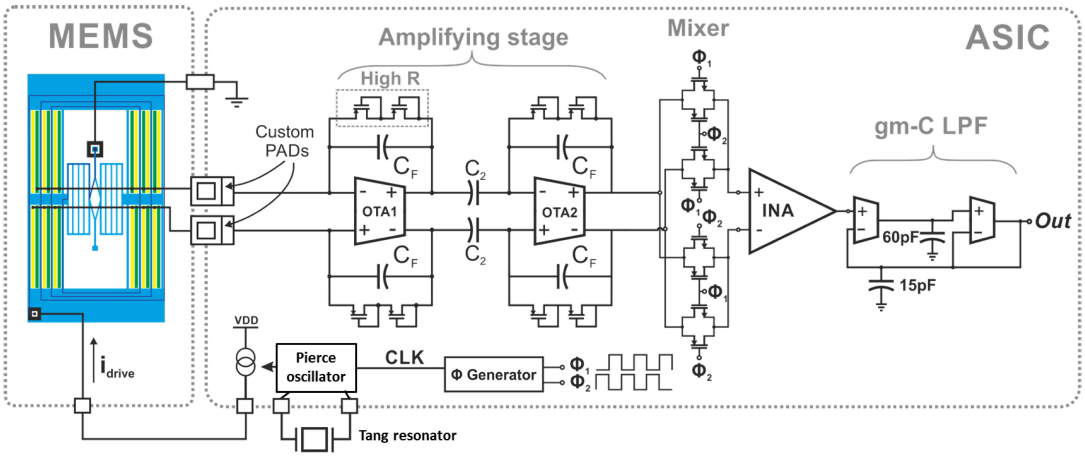

Fig. 6. Schematic representation of the driving and the readout circuits.

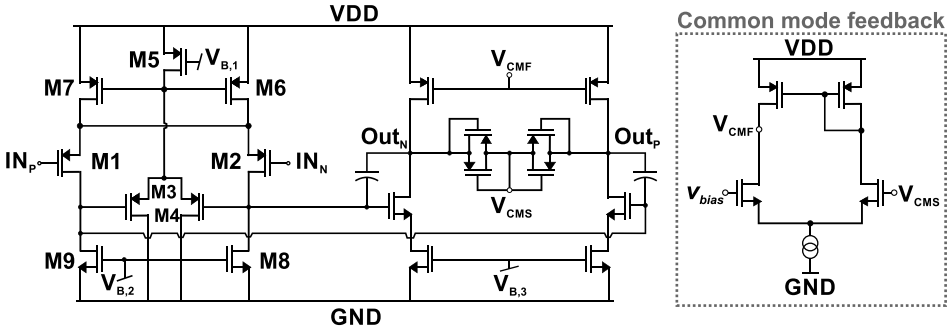

Fig. 7. Transistor-level implementation of OTA1, with its common-mode feedback network.

the readout electronics. Indeed V_{bias} directly determines the LNA differential output voltage:

$$v_{o1}(t) = \frac{V_{bias}}{C_F} C_d(t), \tag{5}$$

where C_d is the differential capacitance variation of the MEMS structure, and C_F = 25 fF is the feedback capacitance of the amplifier. The C_F value together with V_{bias} sets the gain. The parasitic capacitance between the input and the output of the amplifier is estimated to be less than 2 fF.

This topology was preferred to a transresistance stage not only for its lower noise, but also for the dependence of the gain on a capacitance value, that can be integrated more easily than the high resistance value required by an equivalent transresistance amplifier.

The feedback resistors are implemented by two PMOS transistors biased in sub-threshold region [27], [28] providing a resistance R_{PMOS} larger than 10 GΩ and a closed loop cut-off frequency approximately equal to:

$$f_{cut} = \frac{1}{2\pi R_{PMOS} C_F} \approx 600\,\text{Hz}. \tag{6}$$

This frequency corresponds to the lower pole of both the transfer function between the input current and the output voltage of the LNA (a low-pass pole) and of the voltage transfer function of the second amplifier (a high-pass pole). Setting the pole value below 1 kHz, the differential capacitance variations around 20 kHz ($C_d(t) = B \cdot S_m \sin(2\pi f_d t)$) are effectively amplified as in Eq. 5. Furthermore, f_{cut} is also the low-pass cut-off frequency of the feedback pseudo-resistor noise, whose contribution in the proximity of the sensor operating frequency is then negligible.

The internal architecture of the first Operational Transconductance Amplifier (OTA1), with its common-mode feedback network, is illustrated in Fig. 7. It relies on a two-stage, Miller-compensated, fully differential topology, with a PMOS input pair to keep flicker noise contribution well below white noise floor.

The first stage adopts a self-consistent common-mode feedback network similar to those presented in [29] and [30], but adapted to a higher power supply by the introduction of a pair of source followers (M3 and M4). These devices shift the gate bias voltage of the tail transistors M6 and M7 by a $V_{GS_{3,4}}$ with respect to the output nodes of the first stage, thus avoiding any transistor to operate in ohmic region. Since M3 and M4 draw less than one tenth of the current of the input transistors, their impact on the power consumption is negligible. With this topology the common mode voltage of the output nodes of the first stage is set by the values of $V_{GS_{3,4}}$ and $V_{GS_{6,7}}$.

The common mode feedback network of the second stage of OTA1 relies on an additional OTA with one input node connected to V_{bias}, which sets the reference voltage for the stator bias condition, and the other one connected to the output of the common-mode sense network V_{CMS}. The latter is implemented by two pairs of cross-coupled PMOS pseudo-resistors. This configuration balances the non-linear variations

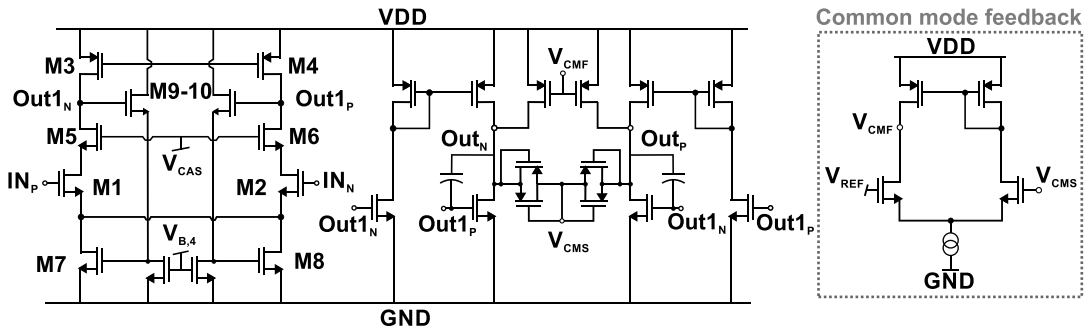

Fig. 8. Transistor-level implementation of OTA2, adopted for the capacitive amplifier, with its common-mode feedback network.

of the pseudo-resistor resistances that occur in presence of a differential signal, suppressing any related common-mode artifact that would otherwise arise at the output node V_{CMS} resulting in a drift of the common mode bias. This effect must be avoided since it could also reduce the output swing and compromise the system sensitivity and linearity.

The stator voltage V_{bias} should be kept as high as possible to guarantee the maximum sensitivity. Within the 3-V supply, it can be raised up to 2 V, the maximum value allowed by the first stage of OTA1 to keep its tail transistors (M6 and M7) in the saturation region and thus to guarantee its correct biasing.

The second amplifying stage, a capacitive amplifier, features a 40-dB gain using an input capacitance of 2.5 pF and a feedback capacitor of 25 fF. Fig. 8 shows its internal implementation (OTA2), which is again a two-stage, Miller-compensated topology.

OTA2 first stage is similar to OTA1, but with the addition of a cascode configuration, implemented by transistors M5-M6. Its role is to reduce the Miller effect across OTA2 input transistors (the Miller effect increases the equivalent capacitance affecting the OTA input nodes, thus lowering the loop-gain and reducing the capacitive amplifier bandwidth). In the proposed topology, instead, the presence of the cascode stage allows to keep the low-pass closed-loop pole of the amplifier at high frequencies without consuming additional current. The same solution could have been adopted also in OTA1 to save power. However, this choice was avoided in this first implementation, to allow tuning the input-pair bias current - from 50 μA to 500 μA - and the common-mode input voltage - from 1.5 V to 2.0 V -, without pushing OTA1 input transistors into the linear region.

The common mode feedback network of the second stage of OTA2 is similar to the one adopted in OTA1. It is used to set the capacitive amplifier output DC voltage close to $V_{REF} = V_{DD}/2 = 1.5$ V, to maximize the swing.

B. Downconversion and Filtering

The amplified signal is then demodulated by a passive mixer, driven by a signal with the same phase and frequency of the AC current flowing into the sensor. This solution allows to downconvert to baseband the magnetic field signal that was modulated at a frequency $f_d = f_0 - \Delta f$ by the drive current.

Finally, the mixer output is converted to a single-ended signal by an instrumentation amplifier before being filtered

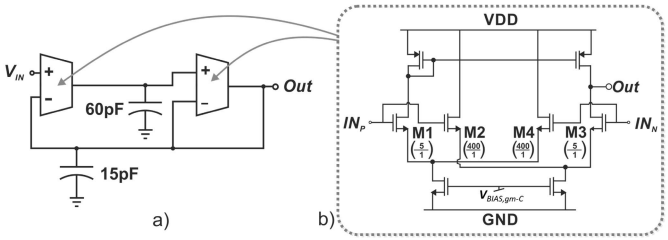

Fig. 9. Schematic view of the g_m-C filter (a), with transistor-level implementation of the OTAs (b).

by a 2^{nd} order g_m-C filter, which is shown in Fig. 9a. A selective filter is desirable in order to eliminate the sensor noise around the resonance. Its low-pass frequency can be regulated between 10 and 150 Hz by tuning the g_m-C filter bias current. To guarantee a full power bandwidth equal to the filter bandwidth, the slew rate of the cell has been boosted by adopting the translinear OTA topology shown in Fig. 9b.

In details, all the transistors of the g_m-C filter OTAs are biased in sub-threshold region. Their nominal tail bias current is equal to 40 nA, only a small fraction of which flows through M1 and M3 (approximately 500 pA, since their aspect ratio is 80 times smaller than that of M2 and M4). For small to moderate input signals, the bandwidth of the filter is determined by the ratio of the transconductance of M1, M3 and the geometric mean of the capacitors C1 and C2. The square root of the ratio between C1 and C2 determines also the quality factor of the poles synthesized by the circuit. Their values were set to 60 pF and 15 pF, respectively, to achieve a 50-Hz bandwidth with a quality factor equal to 0.5, low enough to avoid any peaking. In presence of a large input signal, the transistors connected to the negative swing input turn off, letting the whole tail current charge or discharge the output node and thus providing a slew rate higher than the target value $2\pi \cdot 50$ Hz $\cdot V_{DD}/2$ = 470 V/s.

C. Noise Analysis

The electronic noise at the output of the overall circuit is mainly due to the input differential pair of OTA1. The noise power spectral density at the LNA output is [31]:

$$\overline{E_{n,out}^2} \simeq \overline{E_{n,eq}^2}\left(1+\frac{C_T}{C_F}\right)^2, \tag{7}$$

where C_T is the total capacitance seen from any OTA1 input node to ground and it is given by the sum of the MEMS rotor-to-stator DC capacitance C_0 and the parasitic capacitance C_P. $\overline{E^2_{n,eq}}$ is the input-referred OTA1 noise power spectral density, dominated by the white noise contribution and equal to [32]:

$$\overline{E^2_{n,eq}} = \frac{8k_BT\gamma}{g_{m_{1,2}}}(1+\alpha), \tag{8}$$

where $g_{m_{1,2}}$ is the transconductance of the transistors of the input pair. The coefficient α is the sum of the ratios between the transconductances of the other transistors of OTA1 (mirror, second-stage...) and that of the input pair. To maximize their efficiency g_m/I, the input devices M1 and M2 were biased in weak-inversion, very near to the sub-threshold region. On the contrary, the load transistors M8 and M9 were biased in strong inversion. In such a bias condition, $\alpha \ll 1$ and Eq. 8 can be written as follows:

$$\overline{E^2_{n,eq}} \simeq \frac{4k_BTn^2U_T}{I_{bias}}, \tag{9}$$

where n is the sub-threshold slope coefficient, U_T is the thermal voltage and I_{bias} is the current flowing in each of the input devices.

Based on Eq. 5, the noise contribution of the sensing electronics to the overall resolution can be evaluated in terms of capacitance noise density:

$$\sigma_C \simeq \frac{\sqrt{\overline{E^2_{n,eq}}}\left(1+\frac{C_T}{C_F}\right)C_F}{V_{bias}}, \tag{10}$$

that can be compared to the corresponding sensor contribution expressed in Eq. 4. By substituting the expression in Eq. 9 into Eq. 10, also the capacitive noise contribution can be expressed as a function of the input transistors bias current:

$$\sigma_C \simeq \frac{\sqrt{4k_BTn^2U_T}\left(1+\frac{C_T}{C_F}\right)C_F}{V_{bias}\sqrt{I_{bias}}}, \tag{11}$$

clearly showing that noise reduction requires to raise the bias current I_{bias} quadratically. For this reason it is not convenient, in terms of power efficiency, to bias the input transistors with a current larger than the value strictly needed to keep the amplifier noise contribution comparable or slightly lower than the sensor contribution.

The minimum detectable magnetic field guaranteed by the sensing system can be then obtained by dividing the capacitive noise expressed in Eq. 10 by the sensor sensitivity S_m:

$$\begin{aligned} B_{min} &\simeq \frac{\sqrt{\overline{E^2_{n,eq}}BW}\left(1+\frac{C_T}{C_F}\right)C_F}{S_mV_{bias}} \\ &\simeq \frac{\sqrt{\overline{E^2_{n,eq}}BW}\,(C_P+C_0)}{S_mV_{bias}}. \end{aligned} \tag{12}$$

The simplification above reasonably assumes $C_P + C_0 \gg C_F$. It turns out that the parasitic capacitance C_P must be minimized or at least kept comparable to the MEMS capacitance in order not to amplify the electronic noise. In the present design, the parasitic capacitance has been minimized by directly bonding the two dies and using a refined design of the PADs. Such custom PADs have an overall area of $(60\mu\text{m})^2$, 62% lower than for library PADs; they also feature custom PAD protections (reversely biased diodes) smaller than the library ones; further, they rely only on top-level metals to minimize the parasitic capacitance towards the substrate. These efforts made possible to keep C_T lower than 2.5 pF, compared to a MEMS capacitance of 420 fF, while a standard PAD would have given a C_P capacitance larger than 6 pF, like e.g. in [26].

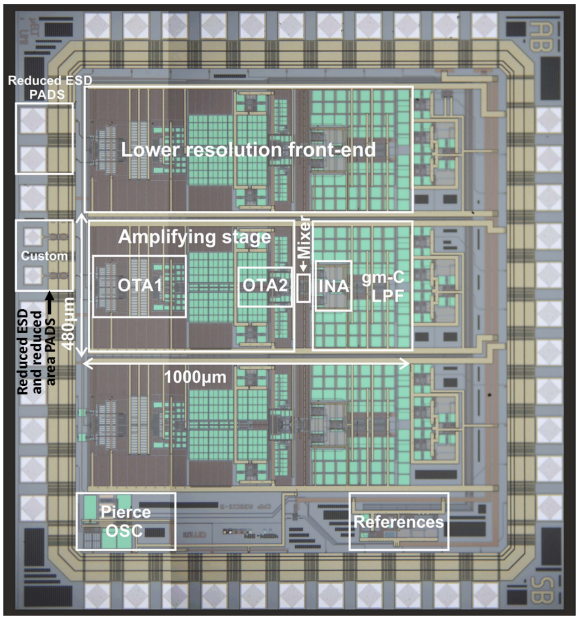

Fig. 10. ASIC die microphotograph with the highlighted circuit blocks. Note the reduced PAD area to minimize parasitic capacitances.

On the other hand, by increasing the bias voltage of the stators, the sensitivity improves without any impact on the electronic noise, thus reducing the equivalent magnetic noise floor due to the amplifier noise. The adoption of input PMOS allows to reliably bias the stators at 2 V while giving negligible flicker noise contribution. With a first stage bias current equal to 50 μA, the electronic capacitive noise contribution was kept to about 30 zF/$\sqrt{\text{Hz}}$, thus comparable to the sensor noise derived in Eq. 4.

IV. Measurements Results

Fig. 10 shows the microphotographs of the ASIC die, fabricated in a 0.35-μm CMOS process from AustriaMicroSystems (AMS). The ASIC core occupies an active area of 0.48 mm^2. The used readout chain is encircled in white, and the reader can note the reduced PAD area with respect to the twin implementation (located just above) used in [26]. The small area taken up by the Pierce oscillator is also highlighted. Fig. 11 shows the two stacked dies wire-bonded onto a socket carrier, mounted on the biasing PCB board which also brings the drive reference when the Pierce oscillator is not used.

A. Sensitivity and Bandwidth

The tests described in this Section were performed using the external drive reference. Fig. 12 shows experimental data,

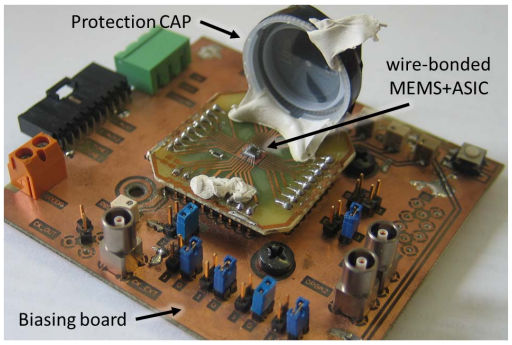

Fig. 11. Photography showing the wire boding of the stacked MEMS and ASIC dies.

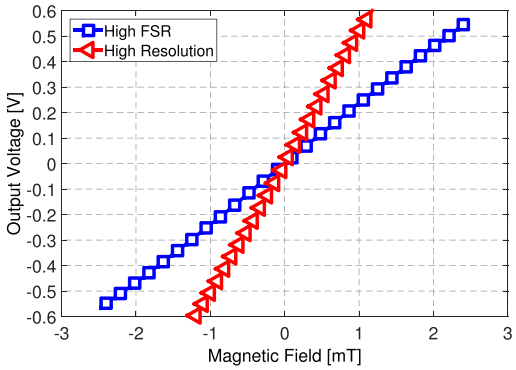

Fig. 12. System sensitivities, evaluated for a 200 Hz mismatch, for two values of the driving current.

where the output voltage is plotted as a function of the input magnetic field, generated with the Helmoltz coil setup.

Measurements were performed biasing the MEMS stators with 2 V and driving the sensor with two different driving currents, to achieve different sensitivity values. The low sensitivity setting, using a driving current $i_0 = 58\ \mu\text{A} = 41\ \mu\text{A}_{rms}$, was chosen to span a maximum full-scale range of ± 2.4 mT, while a high sensitivity configuration, using a driving current of $152\ \mu\text{A} = 107\ \mu\text{A}_{rms}$, was chosen to reach a better resolution, with a lower FSR. The resulting z-axis system sensitivities are found to be 510 mV/mT and 230 mV/mT, respectively. In both configurations, the maximum full-scale range was quoted up to the magnetic field value leading to a 2% linearity error. In both cases the range was limited by the non-linearity of the g_m-C filter, due to its sub-threshold operation.

Thanks to the off-resonance operating mode, the system bandwidth is set by the cut-off frequency of the g_m-C filter. A nominal 50 Hz cut-off can be then guaranteed and tuned between 10 and 150 Hz, avoiding the limit imposed by the intrinsic sensor bandwidth ($\approx$ 20 Hz for this device) [1].

B. System Resolution and Power Consumption

Noise measurements were performed, and both the sole ASIC contribution and the overall sensing system (sensor and ASIC) noise performances were evaluated.

To derive the ASIC noise, the AC driving current was switched off and the signal was demodulated 1 kHz before

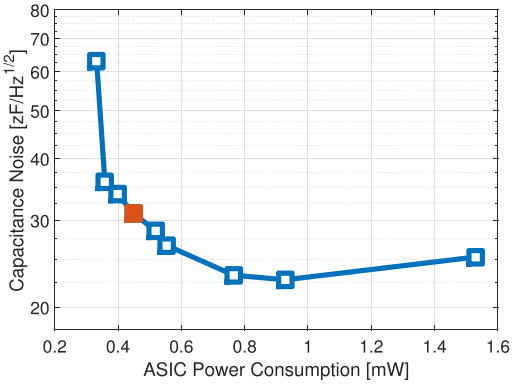

Fig. 13. Input-referred capacitive noise spectral density of the readout electronics as a function of the analog front-end power consumption.

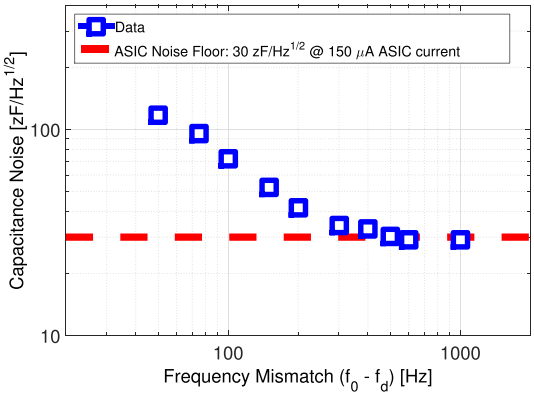

Fig. 14. Equivalent capacitive noise spectral density of the system measured at different frequency mismatches.

resonance, so that the thermomechanical noise contribution is made negligible; noise was measured through the Allan variance method [33] over a 10 s time interval.

Fig. 13 shows the equivalent capacitive white noise due to the analog front-end as a function of its power consumption, which is varied only by changing the current of the first stage of OTA1. Since the electronic noise is mainly due to OTA1 input stage, noise decreases by increasing the bias current (see Eq. 11) at the cost of an increased power consumption. For very high current values, however, noise increases again. This occurs because the input capacitance of the differential pair increases once the transistors leave the sub-threshold region to enter the strong inversion region. Taking a nominal bias current of 50 μA for the first stage of OTA1, the power consumption of the whole front-end (including the mixer and the g_m-C filter) is equal to 450 μW, with an input-referred capacitive noise of 30 zF/$\sqrt{\text{Hz}}$ (see the point marked in orange in Fig. 13).

Fig. 14 shows the noise performance of the overall system (MEMS and ASIC), evaluated in terms of capacitive noise spectral density as a function of the mismatch between the drive and the resonance frequency. Here, the power consumption of the ASIC is the nominal value (450 μW). As the frequency mismatch is reduced, the MEMS thermomechanical noise contribution rises. At 200-Hz offset

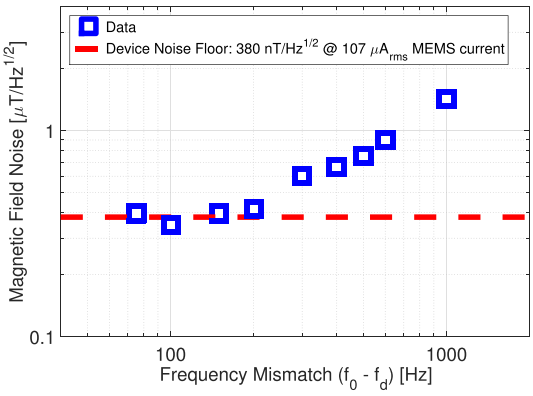

Fig. 15. Input-referred magnetic field noise spectral density of the system measured at different frequency mismatches.

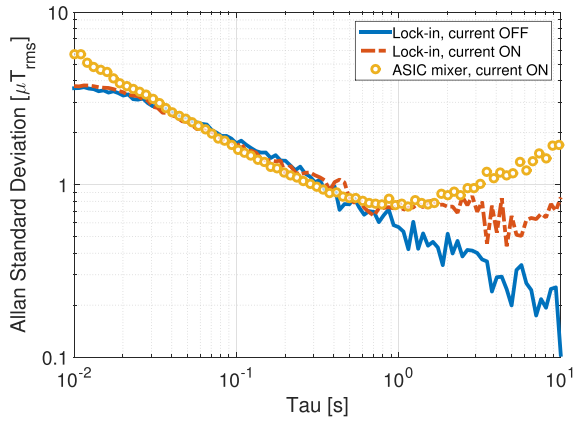

Fig. 16. System noise performance, displayed as input-referred Allan standard deviation, evaluated at 200-Hz mismatch, using a 107-μA$_{rms}$ driving current.

from resonance, the noise contribution of the electronics and the one from the sensor become comparable, resulting into a total equivalent capacitive noise of about 40 zF/$\sqrt{\text{Hz}}$.

The equivalent magnetic field resolution can be obtained by dividing the capacitive noise spectral density by the sensor sensitivity S_m, assuming a driving current of 107 μA_{rms}. Fig. 15 shows the input equivalent noise, quoted as rms magnetic field per unit sensing bandwidth (nT/$\sqrt{\text{Hz}}$), at different frequency mismatches. At frequency mismatches <200 Hz, the sub-400 nT/$\sqrt{\text{Hz}}$ resolution is constant, limited by the MEMS termomechanical noise (the dashed line represents the noise floor as the average of the first four points); at frequency mismatches larger than 200 Hz, the ASIC noise contribution becomes dominant and the resolution begins to degrade.

Fig. 16 shows the input-referred Allan standard deviation graph, evaluated at 200 Hz mismatch, using a 107 μA$_{rms}$ driving current, for different measurement configurations. Solid and dashed curves show the noise performance when the signal is demodulated using an external lock-in amplifier, with AC driving current off and on, respectively. The circle-marker curve represents the Allan deviation using the mixer and the g_m-C filter, as in standard operation. Fig. 16 clearly shows that both the driving current and the mixer introduce a low frequency noise, i.e. an offset drift component, which anyway never exceeds 2 μT, for integration times up to 10 s.

The system power consumption is the sum of both the drive and the electronics currents, being 775 μW and 560 μW when driving at 107 μA$_{rms}$ and 41 μA$_{rms}$, respectively.

C. Perspective for Driving Circuit Integration

The integrated circuit discussed so far and the values of power dissipation given above include the magnetometer readout and the rms value of the Lorentz current, but not the power dissipated in the circuit needed to generate the reference current. The following three considerations guide the choice of the architecture of the driving part of the system:

- the used off-resonance operation mode requires the generation of a current at a reference frequency which is different from the device resonance;
- this frequency difference needs possibly to be stable and immune from environmental changes (mostly temperature), as it directly affects the system sensitivity (Eq. 2);
- the circuit that delivers the Lorentz current should not critically affect the system power consumption.

Considering the first two bullets above, the best option for the implementation of the driving sub-system appears to be the integration, in the same module of the magnetometer, of a high-Q MEMS resonator (e.g. a sample Tang configuration). The resonator should be designed to operate at the required frequency mismatch with respect to the magnetometer. In this way, the resonator will be affected by temperature variations in the same way as the MEMS magnetometer. Indeed, the Young modulus variation with temperature (typically -30 ppm/K) is usually the dominant source of frequency variation with temperature in MEMS devices. To make a numerical example, a $\pm$60 K temperature change around 300 K will nominally cause a $\pm$36 Hz frequency shift for a magnetometer resonating at 20 kHz, and a $\pm$35.64 Hz shift for a resonator with a 19.8 kHz frequency (200 Hz split). In turn, this implies only a $\pm$ 0.18 % mode-split and sensitivity change (see Eq. 2) across the whole temperature range of consumer devices.

Considering the third bullet above and thus the electronics, while few examples of driving circuits for magnetometers implemented with discrete components exist [36], none of them considers power consumption issues. When considering this relevant constraint, a low-power Pierce oscillator topology appears the most suitable one, as it minimizes the number of required stages.

On the same chip of the presented readout circuit, the Pierce oscillator whose transistor-level schematic is shown in Fig. 17 was also integrated [37]. The circuit was dimensioned with both capacitances C_1 and C_2 of 9 pF (including the PAD capacitance), according to standard Pierce circuits design guidelines [38]. The degeneration of M1 is used to shift the DC output of the oscillator close to the threshold of the following inverter, in order to have a 50% duty cycle. The circuit was coupled and tested with a Tang resonator, which however (i) is not integrated in the same die of the magnetometer and (ii) is not provided with tuning electrodes for correct tuning of the frequency difference. Therefore complete tests of the magnetometer driven by the Tang-Pierce

TABLE II

COMPARISON OF THE PRESENTED MAGNETIC FIELD SENSING SYSTEM PERFORMANCE WITH THE STATE-OF-THE-ART

System	Max BW* [Hz]	Driving Current [μA]	Device Length [μm]	FOM [nT·mA/$\sqrt{\text{Hz}}$]	MEMS + IC Power [μW]	Notes
Emmerich [5]	6	1000	1300	1200***	N/A	AM resonant**
Bahreyni [15]	N/A	10000	420	1900	N/A	FM
Kynnarainen [7]	2.5	100	2200	7	N/A	AM resonant** multicoil
Langfelder [8]	43	250	1060	520	N/A	AM resonant**
Li [34]	1.9	8200	1800	140	N/A	AM resonant** 3-axis****
Li [16]	50	1280	370	640	N/A	FM
Langfelder [20]	160	50	1060	170	N/A	AM off-resonance
Kumar [35]	0.2	7200	830	0.02	N/A	AM resonant** + piezoresistive
Li [17]	N/A	4000	1200	80000	N/A	FM micro-leverage
This work	150	150	1400	58	775	AM off-resonance multi-coil

* The final system bandwidth can be selected with proper electronic filtering up to the maximum bandwidth.
** Max BW of AM resonant sensors is calculated as the -3 dB resonant peak width.
*** FOM inferred from other parameters given in the reference.
**** Performance referred to z-axis component only.

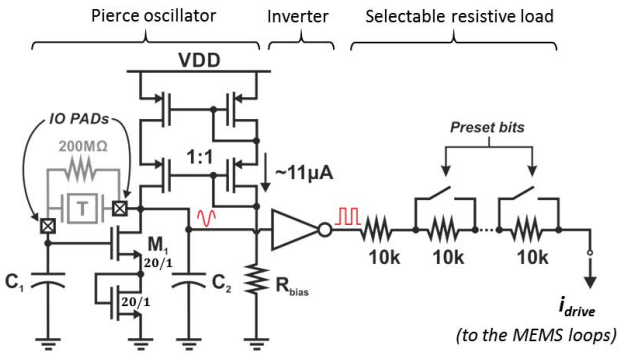

Fig. 17. Transistor level view of the Pierce oscillator. Coupled to a Tang resonator, the circuit implements the driving stage at the oscillation frequency of the resonator, delivering the desired AC current through a resistive load.

pair were not yet possible. A preliminary characterization shows the Pierce circuit correctly delivering the required 107 μA_{rms} current. The current value is set via a selectable resistive load in series to the low resistance (<0.6 kΩ) of the metal loops. The added current consumption by such a Pierce oscillator is 22 μA only (corresponding to 66 μW at the adopted 3-V voltage supply).

It can be thus concluded that the power dissipated in the driving circuit can be made very low (less than 1/10 of the overall consumption). The power dissipation discussed in Section IV.B can be therefore considered representative of the whole magnetic field sensing system.

A design of a Tang resonator with tuning electrodes [39] and positioned in the same die of the magnetometer, to match the intended frequency split and to further complete the system characterization, represents ongoing work.

V. CONCLUSION

A novel z-axis magnetic field sensor, operated in off-resonance mode, has been introduced and fully characterized together with a custom integrated readout circuit. The sensor exploits multiple loop to amplify the sensitivity. It was fabricated in an industrial process currently used for 6-axis inertial sensors, without added magnetic or piezoresistive materials, and without any insulating barrier between metal and polysilicon. Within this class of devices, the performance in terms of resolution normalized to the device current consumption overcomes all the z-axis sensors shown in Table II, also providing bandwidth as large as 50 Hz. The sensor in [7] still shows better resolution performance. However, it adopts an insulating barrier for metal loops, and has a bandwidth inherently limited to 10 Hz only by the -3 dB resonant peak width. The sensor in [35] exploits piezoresistive amplification to improve the resolution, but needs a very large minimum biasing current and has a quite impractical system bandwidth of about 0.2 Hz.

The integrated circuit for Lorentz force MEMS magnetometers readout was designed to keep the electronics noise contributions comparable to the sensor noise. The overall system, including the Lorentz current and the circuit biasing, has a power dissipation of 775 μW. This value increase to 841 μW when a Pierce circuit to provide the reference current is also taken into account. Though the use of custom PADs on the ASIC die, the system resolution is still affected by parasitic capacitances, and further strategies for their minimization will be considered in future works. At the same time, a better design of metal masks, which takes into account the observed over-etch, and the use of high-resistance geometries for the links, should result simultaneously in at least 2-fold improved sensitivity and resolution.

REFERENCES

[1] S. Brenna *et al.*, "A low-noise sub-500 μW Lorentz force based integrated magnetic field sensing system," in *Proc. 28th IEEE Int. Conf. Micro Electro Mech. Syst. (MEMS)*, Jan. 2015, pp. 932–935.

[2] S. Tumański, *Thin Film Magnetoresistive Sensors*. New York, NY, USA: Taylor & Francis, 2001.

[3] W.-M. Lai, F.-M. Hsu, W.-L. Sung, R. Chen, and W. Fang, "Monolithic integration of micro magnetic pillar array with anisotropic magneto-resistive (AMR) structure for out-of-plane magnetic field detection," in *Proc. 28th IEEE Int. Conf. Micro Electro Mech. Syst. (MEMS)*, Jan. 2015, pp. 901–904.

[4] C. Sander *et al.*, "Fully symmetric vertical Hall devices in CMOS technology," in *Proc. IEEE SENSORS*, Nov. 2013, pp. 1–4.

[5] H. Emmerich, M. Schofthaler, and U. Knauss, "A novel micromachined magnetic-field sensor," in *Proc. 12th IEEE Int. Conf. Micro Electro Mech. Syst. (MEMS)*, Jan. 1999, pp. 94–99.

[6] M. J. Thompson and D. A. Horsley, "Parametrically amplified MEMS magnetometer," in *Proc. Int. Solid-State Sens., Actuators, Microsyst. Conf. TRANSDUCERS*, Jun. 2009, pp. 1194–1197.

[7] J. Kyynäräinen *et al.*, "A 3D micromechanical compass," *Sens. Actuators A, Phys.*, vol. 142, no. 2, pp. 561–568, 2008.

[8] G. Langfelder, C. Buffa, A. Frangi, A. Tocchio, E. Lasalandra, and A. Longoni, "Z-axis magnetometers for MEMS inertial measurement units using an industrial process," *IEEE Trans. Ind. Electron.*, vol. 60, no. 9, pp. 3983–3990, Sep. 2013.

[9] M. Li and D. A. Horsley, "Offset suppression in a micromachined Lorentz force magnetic sensor by current chopping," *J. Microelectromech. Syst.*, vol. 23, no. 6, pp. 1477–1484, Dec. 2014.

[10] L. Prandi *et al.*, "A low-power 3-axis digital-output MEMS gyroscope with single drive and multiplexed angular rate readout," in *IEEE Int. Solid-State Circuits Conf. Dig. Tech. Papers (ISSCC)*, Feb. 2011, pp. 104–106.

[11] G. Langfelder and A. Tocchio, "Operation of Lorentz-force MEMS magnetometers with a frequency offset between driving current and mechanical resonance," *IEEE Trans. Magn.*, vol. 50, no. 1, Jan. 2014, Art. ID 4700106.

[12] S. Sonmezoglu, M. Li, and D. A. Horsley, "Force-rebalanced Lorentz force magnetometer based on a micromachined oscillator," *Appl. Phys. Lett.*, vol. 106, no. 9, p. 093504, 2015.

[13] G. Wu, D. Xu, B. Xiong, D. Feng, and Y. Wang, "Resonant magnetic field sensor with capacitive driving and electromagnetic induction sensing," *IEEE Electron Device Lett.*, vol. 34, no. 3, pp. 459–461, Mar. 2013.

[14] D. Ettelt, P. Rey, G. Jourdan, A. Walther, P. Robert, and J. Delamare, "3D magnetic field sensor concept for use in inertial measurement units (IMUs)," *J. Microelectromech. Syst.*, vol. 23, no. 2, pp. 324–333, Apr. 2014.

[15] B. Bahreyni and C. Shafai, "A resonant micromachined magnetic field sensor," *IEEE Sensors J.*, vol. 7, no. 9, pp. 1326–1334, Sep. 2007.

[16] M. Li, S. Sonmezoglu, and D. A. Horsley, "Extended bandwidth Lorentz force magnetometer based on quadrature frequency modulation," *J. Microelectromech. Syst.*, vol. 24, no. 2, pp. 333–342, Apr. 2015.

[17] M. Li, S. Nitzan, and D. A. Horsley, "Frequency-modulated Lorentz force magnetometer with enhanced sensitivity via mechanical amplification," *IEEE Electron Device Lett.*, vol. 36, no. 1, pp. 62–64, Jan. 2015.

[18] C. Acar, A. R. Schofield, A. A. Trusov, L. E. Costlow, and A. M. Shkel, "Environmentally robust MEMS vibratory gyroscopes for automotive applications," *IEEE Sensors J.*, vol. 9, no. 12, pp. 1895–1906, Dec. 2009.

[19] G. Langfelder, S. Dellea, A. Berthelot, P. Rey, A. Tocchio, and A. F. Longoni, "Analysis of mode-split operation in MEMS based on piezoresistive nanogauges," *J. Microelectromech. Syst.*, vol. 24, no. 1, pp. 174–181, Feb. 2015.

[20] G. Langfelder, G. Laghi, P. Minotti, A. Tocchio, and A. Longoni, "Off-resonance low-pressure operation of Lorentz force MEMS magnetometers," *IEEE Trans. Ind. Electron.*, vol. 61, no. 12, pp. 7124–7130, Dec. 2014.

[21] M. F. Zaman, A. Sharma, Z. Hao, and F. Ayazi, "A mode-matched silicon-yaw tuning-fork gyroscope with subdegree-per-hour Allan deviation bias instability," *J. Microelectromech. Syst.*, vol. 17, no. 6, pp. 1526–1536, Dec. 2008.

[22] B. R. Simon, A. A. Trusov, and A. M. Shkel, "Anti-phase mode isolation in tuning-fork MEMS using a lever coupling design," in *Proc. IEEE Sensors*, Oct. 2012, pp. 1–4.

[23] M. Li, V. T. Rouf, M. J. Thompson, and D. A. Horsley, "Three-axis Lorentz-force magnetic sensor for electronic compass applications," *J. Microelectromech. Syst.*, vol. 21, no. 4, pp. 1002–1010, Aug. 2012.

[24] V. Kempe, *Inertial MEMS: Principles and Practice*. Cambridge, U.K.: Cambridge Univ. Press, 2011.

[25] A. Frangi, A. Ghisi, and L. Coronato, "On a deterministic approach for the evaluation of gas damping in inertial MEMS in the free-molecule regime," *Sens. Actuators A, Phys.*, vol. 149, no. 1, pp. 21–28, 2009.

[26] S. Brenna, P. Minotti, G. Langfelder, A. Bonfanti, A. Longoni, and A. Lacaita, "Low-noise, low-power and extended bandwidth MEMS magnetic field sensing system," in *Proc. 3rd CSCCA*, Nov. 2014, pp. 13–21.

[27] R. R. Harrison, "A low-power, low-noise CMOS amplifier for neural recording applications," in *Proc. IEEE Int. Symp. Circuits Syst. (ISCAS)*, vol. 5. May 2002, pp. 197–200.

[28] A. Bonfanti *et al.*, "A multi-channel low-power IC for neural spike recording with data compression and narrowband 400-MHz MC-FSK wireless transmission," in *Proc. ESSCIRC*, Sep. 2010, pp. 330–333.

[29] W.-S. Liew, X. Zou, and Y. Lian, "A 0.5-V 1.13-μW/channel neural recording interface with digital multiplexing scheme," in *Proc. ESSCIRC*, Sep. 2011, pp. 219–222.

[30] M. Chae, J. Kim, and W. Liu, "Fully-differential self-biased bio-potential amplifier," *Electron. Lett.*, vol. 44, no. 24, pp. 1390–1391, Nov. 2008.

[31] R. R. Harrison and C. Charles, "A low-power low-noise CMOS amplifier for neural recording applications," *IEEE J. Solid-State Circuits*, vol. 38, no. 6, pp. 958–965, Jun. 2003.

[32] B. Razavi, *Design of Analog CMOS Integrated Circuits*, 1st ed. New York, NY, USA: McGraw-Hill, 2001.

[33] M. Vagner, P. Benes, and Z. Havranek, "Experience with Allan variance method for MEMS gyroscope performance characterization," in *Proc. IEEE Int. Instrum. Meas. Technol. Conf. (I2MTC)*, May 2012, pp. 1343–1347.

[34] M. Li *et al.*, "Single-structure 3-axis Lorentz force magnetometer with sub-30 nT/$\sqrt{}$HZ resolution," in *Proc. IEEE 27th Int. Conf. Micro Electro Mech. Syst. (MEMS)*, Jan. 2014, pp. 80–83.

[35] V. Kumar, M. Mahdavi, X. Guo, E. Mehdizadeh, and S. Pourkamali, "Ultra sensitive Lorentz force MEMS magnetometer with pico-tesla limit of detection," in *Proc. 28th IEEE Int. Conf. Micro Electro Mech. Syst. (MEMS)*, Jan. 2015, pp. 204–207.

[36] S. M. Dominguez-Nicolas, R. Juarez-Aguirre, P. J. Garcia-Ramirez, and A. L. Herrera-May, "Signal conditioning system with a 4–20 mA output for a resonant magnetic field sensor based on MEMS technology," *IEEE Sensors J.*, vol. 12, no. 5, pp. 935–942, May 2012.

[37] A. A. Seshia, W. Z. Low, S. A. Bhave, R. T. Howe, and S. Montague, "Micromechanical pierce oscillator for resonant sensing applications," in *Proc. Int. Conf. Modeling Simulation Microsyst. Tech.*, 2002, pp. 162–165.

[38] E. A. Vittoz, M. G. R. Degrauwe, and S. Bitz, "High-performance crystal oscillator circuits: Theory and application," *IEEE J. Solid-State Circuits*, vol. 23, no. 3, pp. 774–783, Jun. 1988.

[39] H. G. Barrow *et al.*, "A real-time 32.768-kHz clock oscillator using a 0.0154-mm^2 micromechanical resonator frequency-setting element," in *Proc. IEEE Int. Freq. Control Symp. (FCS)*, May 2012, pp. 1–6.